

PanoGrounder: Bridging 2D and 3D with Panoramic Scene Representations for VLM-based 3D Visual Grounding

Seongmin Jung^{1*} Seongho Choi^{1*} Gunwoo Jeon¹ Minsu Cho² Jongwoo Lim¹

¹Seoul National University ²Pohang University of Science and Technology (POSTECH)

{sm18570, sh.choi, gunw0, jongwoo.lim}@snu.ac.kr mscho@postech.ac.kr

<https://choiseongho-h.github.io/PanoGrounder>

Abstract

3D Visual Grounding (3DVG) is a critical bridge from vision-language perception to robotics, requiring both language understanding and 3D scene reasoning. Traditional supervised models leverage explicit 3D geometry but exhibit limited generalization, owing to the scarcity of 3D vision-language datasets and the limited reasoning capabilities compared to modern vision-language models (VLMs). We propose **PanoGrounder**, a generalizable 3DVG framework that couples multi-modal panoramic representation with pretrained 2D VLMs for strong vision-language reasoning. Panoramic renderings, augmented with 3D semantic and geometric features, serve as an intermediate representation between 2D and 3D, and offer two major benefits: (i) they can be directly fed to VLMs with minimal adaptation and (ii) they retain long-range object-to-object relations thanks to their 360-degree field of view. We devise a three-stage pipeline that places a compact set of panoramic viewpoints considering the scene layout and geometry, grounds a text query on each panoramic rendering with a VLM, and fuses per-view predictions into a single 3D bounding box via lifting. Our approach achieves state-of-the-art results on ScanRefer and Nr3D, and demonstrates superior generalization to unseen 3D datasets and text rephrasings.

1. Introduction

3D Visual Grounding (3DVG) aims to localize a target object in a 3D scene from a free-form natural language query, sitting at the interface of natural language understanding and 3D scene understanding [2, 9]. As a core capability for embodied AI, 3DVG underpins applications in augmented reality, vision-language navigation, and robotic perception and manipulation [3]. The task consists of two components: (i) *language understanding* to extract attributes and relations from the description, and (ii) *3D scene understanding*

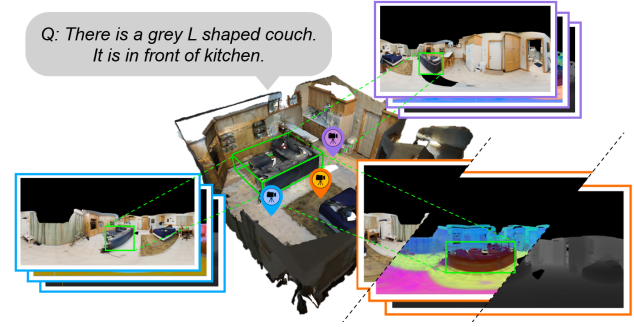


Figure 1. **Overview.** Given a free-form text query and a 3D scene, **PanoGrounder** outputs a single 3D bounding box that localizes the referred object. Panoramic renderings serve as a 2D-3D interface with two functions: providing 360° scene context and spatial relations between objects, and enabling direct transfer of 2D VLMs' language understanding to 3D tasks from the panoramas and the 3D model.

to ground those cues in metric geometry to find the target object [31].

Traditional 3DVG systems typically employ separate encoders for text and point clouds, followed by a cross-modal fusion transformer [31]. By directly operating on the metric 3D scene, these models have achieved strong performance on standard benchmarks [2, 9]. Nevertheless, this design has two major limitations: (i) *restricted language comprehension* and (ii) *limited 3D generalization*. On the language side, most works rely on BERT [12] or CLIP [40]-style encoders, which offer more limited compositional and spatial reasoning capabilities than modern VLMs [28, 33, 36, 44, 55, 57], making paraphrases and relation-heavy descriptions difficult to handle. On the 3D side, these models are trained from scratch on limited-scale 3DVG datasets [2, 9], which constrains their generalization to scenes, categories, and linguistic expressions outside the training distribution.

To leverage stronger language reasoning, recent works introduce VLMs into the 3DVG pipeline in various ways.

*Equal contribution.

However, transferring 2D pretrained capacity to 3D remains non-trivial. (i) Zero-shot VLM-based methods [29, 49] use multi-turn conversations to inject 3D context and obtain grounding result, but often suffer from unreliable view selection and are infeasible to fine-tune. (ii) Fine-tuning-based approaches [47, 59] integrate VLMs as submodules within larger 3D networks and attach task-specific decoding heads for bounding box prediction. While effective in some settings, these designs increase architectural complexity, require additional supervision, and still rely on task-specific interfaces to bridge 2D and 3D modalities. This calls for a simpler and efficient intermediate representation that connects 2D VLMs with 3D reasoning.

In this paper, we introduce **PanoGrounder**, which uses multi-modal panoramic renderings as an explicit intermediate representation between 2D and 3D modalities. By covering a 360° field of view, this panoramic representation preserves holistic object-to-object spatial relations within a single image while remaining fully compatible with pretrained VLMs. We devise a three-stage pipeline: (i) we select a compact set of panoramic viewpoints and render multi-modal panoramas—RGB, semantic [37], and range—for richer contextual cues; (ii) a pretrained VLM processes each panorama to predict a 2D bounding box in pixel coordinates; and (iii) we lift each panorama’s 2D grounding output into metric 3D space and fuse them across views. To inject 3D-aware cues from the semantic and range renderings, we augment the VLM with a lightweight Adapter [58] that projects *semantic* and *geometric* information, and we fine-tune this adapter in the panoramic domain.

PanoGrounder exhibits strong generalization across datasets. By mapping 3D scenes into 2D panoramic renderings, it suppresses domain-specific artifacts of each 3D dataset (e.g., point cloud cleaning heuristics or sensor-dependent noise) and provides much denser visual signals. Combined with the stronger language understanding of modern VLMs, this leads to more robust grounding under distribution shifts.

We evaluate on the standard 3DVG benchmarks, ScanRefer [9] and ReferIt3D (Nr3D, Sr3D) [2]. Our method achieves state-of-the-art performance on ScanRefer and Nr3D, and consistently ranks among the top-performing approaches on Sr3D. We further assess (i) *scene generalization* on ARKitScenes+SceneVerse [5, 24] and 3RScan+RIORefer [35, 43] and (ii) *text generalization* with a modified version of ScanRefer queries. Across all settings, our method exhibits strong generalization when compared to fully supervised methods.

Our main contributions are as follows:

- We introduce **PanoGrounder**, which treats panoramic renderings as a 2D–3D interface for pretrained 2D VLMs. This design preserves scene-wide context while enabling powerful vision-language reasoning with only minimal

modifications around the VLM.

- PanoGrounder effectively injects *semantic* and *geometric* features into the VLM’s vision encoder via a multi-modal feature adapter, and provides distance-aware supervision through an Earth-Mover’s Distance (EMD) loss.
- Our approach achieves state-of-the-art performance on ScanRefer and Nr3D. It further demonstrates strong generalization to unseen scenes and diverse text rephrasings.

2. Related Work

2.1. 3D Visual Grounding

Two-stage vs. one-stage. Traditional supervised methods use separate encoders for text and 3D scenes and fuse them via a cross-modal module. Two-stage approaches [1, 2, 4, 8–10, 19, 20, 51, 52, 62, 63] follow a proposal-and-selection paradigm: a 3D detector/segmentor [38] first proposes candidate objects, and the model selects the one matching the query. SAT [51] and LAR [4] distill rich 2D priors into 3D representations, while ViewSRD [19] improves text understanding by decomposing complex queries into simpler clauses using an LLM before grounding. In contrast, one-stage methods [22, 23, 34, 39, 46, 48] directly regress 3D bounding boxes conditioned on the query. BUTD-DETR [22] adopts a DETR-style encoder-decoder [7] architecture with language and objectness guidance, whereas MCLN [39] extends with two parallel decoders for box-level and mask-level prediction, enhancing overall localization consistency.

2D-based 3DVG. Without relying on a global 3D scene point cloud, a line of works performs 3DVG directly from one or a small set of RGB(-D) views. Refer-it-in-RGBD [32] operates on single-view RGB-D and employs a coarse-to-fine framework to recover the full 3D extent of partially observed targets. Mono3DVG [56] tackles single-view monocular RGB in autonomous-driving scenes, leveraging a lightweight depth predictor. Recent zero-shot approaches [29, 49, 50, 53] prompt an LLM/VLM with multi-turn instructions combining images and text to inject scene context. These methods reduce 3D annotation cost but typically require precise view selection, limiting reliability in complex, cluttered scenes. For zero-shot variants in particular, task-aligned fine-tuning is often infeasible because they are API-based or rely on frozen VLMs.

2.2. Multi-Modal 3D Perception

A complementary line of work jointly trains models on multiple tasks, such as 3D visual grounding, 3D scene captioning, and Visual Question Answering (VQA), to align 3D and language spaces. [30, 62, 63] adopt transformer-based alignment where task-specific heads branch from a shared backbone. UniVLG [23] further leverages abundant 2D data via a neural 2D-to-3D lifting model to trans-

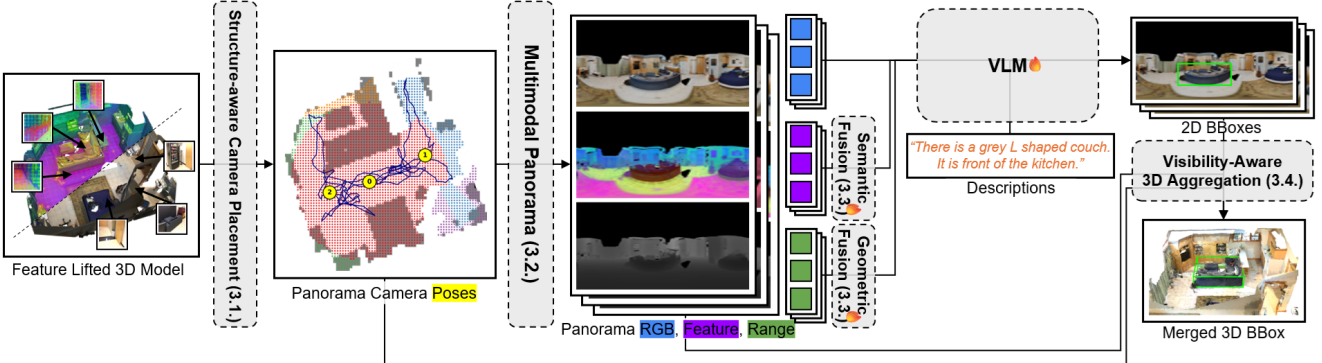


Figure 2. **Overall pipeline of PanoGrounder.** We first select a compact set of informative panoramic viewpoints via Structure-aware Camera Placement and render multi-modal panoramas (RGB, lifted semantic features, and range). Each view is processed by an off-the-shelf VLM augmented with our multi-modal feature adapter to produce 2D bounding boxes from the text query. Finally, per-view 2D predictions are lifted and fused with visibility-aware multi-view aggregation to yield a single 3D bounding box for the referred object.

fer supervision into 3D. Beyond supervised alignment, 3D-R1 [21] explores RLHF-style policy optimization to refine instruction following in 3D contexts. Recently, Multi-modal Large Language Models (MLLMs) have been investigated by feeding 3D-aware tokens into pretrained VLM backbones [33]. Scene-LLM [16] forms hybrid voxel-point tokens from multi-view features [40] and linearly projects them into the LLM space. Chat-Scene [18] uses object proposals with per-instance Object Identifier tokens to fuse 2D/3D object features for unified object-token reasoning. LLaVA-3D [60] augments 2D patch tokens with 3D position embeddings to create 3D-aware patches for the LLM.

3. Method

We assume the 3D scene is given as a renderable representation (e.g., a triangle mesh or 3D Gaussian Splatting [25]). Given a 3D scene and a text query, our goal is to predict a 3D bounding box of the referred object. We use panoramic renderings of the 3D scene as an intermediate representation between 2D and 3D. As illustrated in Fig. 2, our framework consists of three stages. First, we select a small number of informative viewpoints via structure-aware camera placement (Sec. 3.1), and render multi-modalities for VLM stage (Sec. 3.2). Second, we feed each rendering into a trainable VLM equipped with our multi-modal feature adapter to produce 2D bounding box predictions (Sec. 3.3). Finally, we lift per-view 2D predictions to 3D using visibility-aware multi-view fusion to obtain a 3D bounding box (Sec. 3.4). We apply Earth Mover’s Distance (EMD) loss along with traditional cross-entropy for numerical distance-aware supervision (Sec. 3.5).

3.1. Structure-aware Camera Placement

Panoramic cameras capture an omnidirectional view of the scene, bypassing the need to predict a specific viewing ori-

entation, so we only select *locations*. We start by estimating the floor via RANSAC [14] and set the height z to the average height of the raw cameras used during scene reconstruction. We then place a regular grid $\mathcal{G} = \{p_i\}$ with $h=10$ cm spacing across the scene’s 2D floor footprint, and treat each grid point p_i as a candidate camera location.

Camera sampling score. To score each candidate $p \in \mathcal{G}$, we construct three factors:

- **Ray coverage** $A(p) \in [0, 1]$: fraction of other grid points visible from p within $r_{\max}=3$ m. This factor is used to include as much area as possible. A point is counted as visible if it projects onto the panoramic image plane without intersecting obstacles.
- **Distance-to-surface** $D_{\text{surf}}(p)$: Euclidean distance from p to the nearest scene geometry (walls or furniture). Closer placements yield oversized foregrounds, panoramic distortion, and occlusions, so larger distances are preferred.
- **Distance-to-trajectory** $D_{\text{traj}}(p)$: Euclidean distance from p to the nearest raw RGB camera center (if available). Smaller values encourage consistency with the capture trajectory, which empirically improves reconstruction fidelity and panoramic image quality.

Score and selection. We rank candidates using

$$S(p) = \frac{A(p) D_{\text{surf}}(p)}{D_{\text{traj}}(p) + \varepsilon}, \quad \varepsilon = 10^{-3}, \quad (1)$$

which favors locations that (i) cover a wide area, (ii) are not too close to obstacles, and (iii) stay close to the input trajectory. Starting from the highest-scoring point, we greedily select cameras. Once a camera is selected, all grid points visible from it are marked as ‘covered’, effectively setting their contribution to the ray coverage $A(p)$ to zero for all remaining candidates. This sequential selection is repeated until at least 90% of the scene’s grid points are covered. We provide ablations on this strategy in the supplementary.

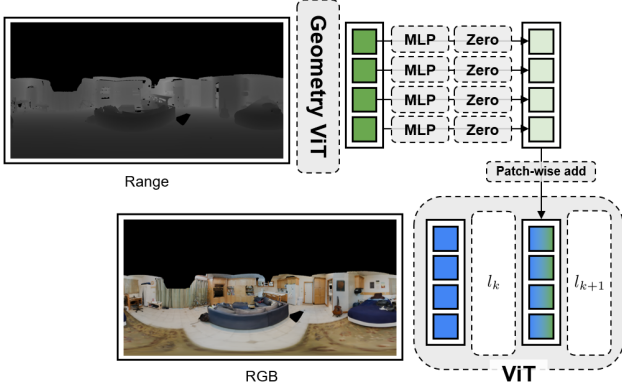


Figure 3. **Multi-Modal Feature Adapter.** We inject panoramic *geometry* (range) and *semantic* (multi-view) features into selected ViT layers of the VLM. Each modality is processed by a lightweight adapter (2-layer MLP followed by a 1×1 convolution), and the resulting output is added patch-wise to the ViT tokens. The 1×1 convolution weights and bias are initialized to zero.

3.2. Multi-Modal Panorama

For each selected viewpoint, indexed by k , we render a panoramic image $I_k \in \mathbb{R}^{H \times W \times 3}$ using equirectangular projection (ERP). However, even with these well-placed viewpoints, relying on RGB alone is inadequate for 3DVG due to (i) occlusions in cluttered indoor scenes and (ii) the absence of explicit 3D information for spatial reasoning. We therefore obtain *geometric* and *semantic* feature maps from the same panoramic cameras.

Geometric feature map. For each panoramic camera, we render a range (depth) map D . D is fed to a lightweight pretrained ViT to obtain a geometric feature map $\mathbf{f}_{\text{geo}} \in \mathbb{R}^{N_f \times d_{\text{geo}}}$, where N_f represents the feature sequence length (e.g., $h \times w$). Its spatial layout, represented as a sequence of length N_f , matches that of the RGB feature map.

Multi-view fused semantic feature map. We extract dense semantic feature maps $\mathbf{f}_{\text{raw},i}$ from a frozen ViT encoder [37] applied to the original RGB views of the dataset. Using known intrinsics and extrinsics, each $\mathbf{f}_{\text{raw},i}$ is unprojected to 3D and their d_{sem} -dimensional descriptors are assigned to visible mesh vertices. Features from all views are aggregated by averaging to form an augmented 3D semantic field \mathbf{F} that is robust to occlusion. This augmented field \mathbf{F} is pre-computed once per scene. Finally, \mathbf{F} is *re-projected* onto the selected panoramic cameras to produce a semantic feature map $\mathbf{f}_{\text{sem}} \in \mathbb{R}^{N_f \times d_{\text{sem}}}$.

3.3. Multi-Modal Feature Adapter

We fuse RGB with panoramic *geometric* and *semantic* features by injecting them into the VLM’s vision encoder via lightweight adapters (Fig. 3). For both modalities we use the same adapter design: a 2-layer MLP followed by a

1×1 convolution whose weights and bias are initialized to zero, following Zero-Convolution [58]. At initialization, the adapter output is exactly zero, so the VLM behaves identically to its pretrained form. Fine-tuning lets the adapters encode task-relevant signals without distorting the original representation space. Geometric features are injected into *mid-level* layers ($l \in [L/3, 2L/3]$) to provide a spatial scaffold, whereas semantic features are injected into *later* layers ($l \in [2L/3, L]$) to supply high-level contextual cues.

$$\mathbf{X}_{l,n} \leftarrow \mathbf{X}_{l,n} + \text{ZeroConv}_m(\text{MLP}_m(\mathbf{f}_{m,n})) \quad (2)$$

This enables the VLM to reason over complex panoramic scenes and robustly ground objects, even under occlusion and panoramic distortion.

3.4. Visibility-Aware 3D Aggregation

For each selected panoramic camera s , we have an RGB panorama I_s and a range map D_s . Given the text query, the VLM predicts a 2D bounding box b_s . We also assume known extrinsics obtained from Structure-aware Camera Placement. This pipeline serves to filter out incorrect individual 2D bounding box predictions by leveraging multi-view consistency.

Step 1: Mask-to-3D lifting. Given I_s and b_s , we query a segmentation model (e.g., SAM [26]) to obtain a mask M_s . Masked pixels are unprojected with D_s and mapped to world coordinates, yielding the per-view point set \mathcal{P}_s .

Step 2: Best-view selection. For each s , project \mathcal{P}_s into every other view $t \neq s$ and obtain the tight 2D box $\hat{b}_{s \rightarrow t}$ around the projected points. Define the cross-view consistency score

$$\text{score}(s) = \sum_{t \in \mathcal{S} \setminus \{s\}} \text{IoU}(\hat{b}_{s \rightarrow t}, b_t),$$

and select $s^* = \arg \max_s \text{score}(s)$ as the *best view*. This favors boxes that are geometrically consistent across views.

Step 3: Multi-view fusion. We merge all per-view point sets $\mathcal{P} = \bigcup_{s \in \mathcal{S}} \mathcal{P}_s$ and denoise. We then project the denoised points into the best view s^* and retain only points whose projections lie inside b_{s^*} , producing the visibility-filtered set \mathcal{P}_{vis} . Fit an axis-aligned bounding box (AABB) to \mathcal{P}_{vis} to obtain the final 3D box.

For ReferIt3D-style evaluation, where candidate boxes are provided, we also support a *two-stage* variant for fair comparison, without changing the core modules (details in the supplementary).

3.5. Training Objective

For each selected viewpoint, we also render an instance-ID map for each camera location, along with RGB and feature maps. We then construct image-text-object triplets by

pairing panoramas with referring expressions and target instance identifiers from the original datasets.

Cross-Entropy. We supervise the autoregressive decoder with standard token-level cross-entropy under teacher forcing. Each bounding box coordinate is normalized to $[000, 999]$, discretized into $N = 3$ digits, and predicted as a sequence of digit tokens $\{0, \dots, 9\}$.

Earth Mover’s Distance (EMD) Loss. Inspired by [41] Treating each digit as a categorical label makes the cross-entropy loss insensitive to numerical proximity: for a ground-truth digit 5, predicting 6 and 9 are penalized equally. To inject awareness of the underlying numerical orderings, we introduce an auxiliary EMD loss (1-Wasserstein distance) [15] over the digit distributions.

For the i -th digit, let $D_i \in \{0, \dots, 9\}$ be the ground-truth digit and $P^{(i)}(d)$ the predicted probability for digit d . We define

$$L_{\text{EMD}}^{(i)} = W_i \sum_{d=0}^9 P^{(i)}(d) |D_i - d|, \quad (3)$$

where W_i is a place-value weight (e.g., $10^2, 10^1, 10^0$ for hundreds/tens/ones), applied for numerical plausibility. This encourages probability mass to concentrate near the correct digit and penalizes larger deviations more heavily.

Total loss. For a coordinate represented by N digits, the final objective is

$$L_{\text{total}} = \sum_{i=1}^N \left(L_{\text{CE}}^{(i)} + \lambda L_{\text{EMD}}^{(i)} \right), \quad (4)$$

where $L_{\text{CE}}^{(i)}$ is the cross-entropy loss for the i -th digit and λ balances the two terms. This combination preserves the classification strength of cross-entropy while guiding predictions toward numerically accurate coordinates, yielding more precise and stable bounding boxes.

Geometric QA. We automatically construct auxiliary QA pairs from each panorama and mix them with standard 3DVG dataset during fine-tuning. Specifically, we adopt *language-based distance ordering*: during training, we randomly sample two pixels on a panorama, read their ground-truth depths from the rendered range map, and auto-generate a textual prompt asking which point is closer (or farther). The model answers based on multi-modal feature, aligning geometric reasoning with language without any additional human annotations. We interleave these QA pairs with 3DVG batches at a fixed ratio throughout fine-tuning.

4. Experiments

4.1. Experimental Setup

Datasets. We evaluate on two widely used 3D visual grounding benchmarks: ScanRefer [9] and ReferIt3D

(Nr3D, Sr3D) [2]. ScanRefer annotates 51,583 human-written referring expressions across 800 ScanNet [11] scenes. Nr3D contains 41,503 human utterances over 707 ScanNet scenes spanning 76 object classes, while Sr3D consists of 83,572 template-based spatial descriptions, also referring to 76 object classes.

To assess cross-dataset generalization on Unseen settings, we use ARKitScenes [5] scenes paired with SceneVerse [24] human-written referring expressions only (we exclude automatically generated texts), and 3RScan [43] scenes paired with RIORefer [35] human-written referring expressions. ARKitScenes provides 5,047 captures over 1,661 unique indoor scenes, and SceneVerse includes ARKitScenes among its sources with both human and generated texts. 3RScan comprises 1,482 scans of 478 indoor environments with instance-level annotations, and RIORefer contributes 63,602 human descriptions for 1,380 3RScan scans.

Evaluation Metrics. On ScanRefer, we report Acc@0.25 overall and on the *Unique/Multiple* subsets. *Unique* denotes queries with no same-class distractor, while *Multiple* denotes the presence of same-class distractors. On ReferIt3D (Nr3D, Sr3D), we report Top-1 accuracy overall and on four subsets: *Easy/Hard* (exactly one vs. two or more same-class distractors) and *View-Dependent/View-Independent*, indicating whether resolving the description requires a specific viewpoint (e.g., “left/right”). For the Unseen settings, we report Top-1 accuracy given ground-truth object instances and report *Unique/Multiple* splits using the same criterion as ScanRefer.

Implementation Details. We adopt CogVLM-17B [44] as our 2D grounding backbone, pretrained on large-scale image-text data. We fine-tune the model with LoRA with an Adam optimizer, a cosine decay learning rate schedule (initial learning rate 1×10^{-4}), and a batch size of 64; other optimizer and schedule hyperparameters follow the official CogVLM implementation. For data augmentation, we apply random in-place camera yaw rotations, implemented as horizontal circular shifts (wrap-around) of the panorama. For test time augmentation, we generate four augmented views via horizontal circular shifts and perform independent inference on each.

4.2. 3D Visual Grounding Results

As summarized in Tab. 1, **PanoGrounder** achieves state-of-the-art or top-2 results on most splits, with clear gains on the human-annotated Nr3D and ScanRefer benchmarks. We observe that mixed training on ScanRefer and ReferIt3D (*S+R*) consistently improves performance, as in the case of 3D-VisTA [62], GPS [24], and PQ3D [63]. For a fair comparison, we indicate this in the table by grouping rows into *Single Dataset* and *Multi Dataset* sections.

Table 1. **Evaluation on Nr3D, Sr3D [2], and ScanRefer [9].** To ensure a fair comparison, we group methods by training regime: models trained on a single benchmark versus those trained on mixed datasets (e.g., ScanRefer + ReferIt3D). *S+R* denotes our model trained jointly on ScanRefer and ReferIt3D (Nr3D/Sr3D). For ScanRefer, we report Accuracy@0.25 (IoU). We report results from mesh.

Method	Nr3D					Sr3D					ScanRefer			
	Easy	Hard	VD	VID	Overall	Easy	Hard	VD	VID	Overall	Unique	Multiple	Overall	
Single Dataset	BUTD-DETR [22]	60.7	48.4	46.0	58.0	54.6	68.6	63.2	53.0	67.6	67.0	84.2	46.6	52.2
	ViL3DRel [10]	70.2	57.4	62.0	64.5	64.4	74.9	67.9	63.8	73.2	72.8	81.6	40.3	47.9
	3D-VisTA (<i>scr.</i>) [62]	65.9	49.4	53.7	59.4	57.5	72.1	63.6	57.9	70.1	69.6	77.4	38.7	45.9
	MIKASA [8]	69.7	59.4	65.4	64.0	64.4	78.6	67.3	70.4	75.4	75.2	—	—	—
	GPS (<i>scr.</i>) [24]	67.0	50.9	55.8	59.8	58.7	70.5	63.4	53.1	69.0	68.4	—	—	—
	MCLN [39]	—	—	—	—	59.8	—	—	—	—	68.4	86.9	52.0	57.2
	PQ3D (<i>sg.</i>) [63]	73.3	56.7	60.7	67.0	64.9	<u>78.8</u>	68.2	51.5	<u>76.7</u>	75.6	85.2	46.8	52.8
	LIBA [47]	—	57.2	60.3	—	64.5	—	70.2	61.7	—	75.8	<u>88.8</u>	54.4	59.6
	TSP3D [17]	—	—	—	—	48.7	—	—	—	—	57.1	87.3	51.0	56.5
	VGMamba [61]	—	61.4	—	—	68.3	—	74.4	—	—	81.3	91.9	54.8	60.0
Multi Dataset	ViewSRD [19]	<u>75.3</u>	<u>64.8</u>	<u>68.6</u>	<u>70.6</u>	<u>69.9</u>	78.3	70.6	<u>69.0</u>	76.2	76.0	82.1	37.4	45.4
	Ours	82.2	67.2	70.5	76.3	74.6	81.3	74.2	60.5	80.0	<u>79.1</u>	84.3	55.3	61.0
Multi Dataset	3D-VisTA [62]	72.1	56.7	61.5	65.1	64.2	78.8	71.3	58.9	77.3	76.4	81.6	43.7	50.6
	GPS [24]	72.5	57.8	56.9	67.9	64.9	80.1	71.6	62.8	78.2	77.5	—	—	—
	PQ3D [63]	<u>75.0</u>	<u>58.7</u>	<u>62.8</u>	68.6	<u>66.7</u>	<u>82.7</u>	72.8	62.9	80.5	79.7	<u>86.7</u>	<u>51.5</u>	57.0
	Chat-Scene [18]	—	—	—	—	—	—	—	—	—	—	89.6	47.8	55.5
	LLaVA-3D [60]	—	—	—	—	—	—	—	—	—	—	—	—	50.1
	UniVLG [23]	73.3	57.0	55.1	<u>69.9</u>	65.2	84.4	75.2	<u>66.2</u>	82.4	81.7	—	—	<u>60.7</u>
	Ours (S+R)	84.1	68.4	72.9	77.5	76.1	82.3	<u>74.5</u>	66.6	80.6	<u>79.9</u>	85.0	56.4	62.0

4.2.1. Results on Nr3D and Sr3D [2]

Single-dataset training. On **Nr3D**, our model achieves the best scores across all splits, significantly outperforming prior art ViewSRD by +4.7%. On **Sr3D**, our method ranks at or near the top, yielding Overall 79.1, while VG-Mamba attains the highest result (Overall 81.3). Notably, our model’s superior performance on **Nr3D**, which consists of human-generated referring expressions, highlights its robustness and stronger capability in handling diverse, natural language distributions compared to template-based datasets like **Sr3D**.

Mixed-dataset training (S+R). Training jointly on ScanRefer and ReferIt3D further improves **Nr3D** to new bests. On **Sr3D**, our model remains strongly competitive (Overall 79.9) and is close to the best-reported results (e.g., UniVLG 81.7), ranking mostly second across splits. Notably, these strong results are achieved by training solely on the standard ScanRefer and ReferIt3D datasets, without leveraging additional large-scale datasets or specialized data curation.

4.2.2. Results on ScanRefer [9]

Single-dataset training. Our model attains the best Overall (61.0) and Multiple (55.3) scores, outperforming VG-Mamba (Overall 60.0) and LIBA (Overall 59.6), with particularly strong gains in multi-object scenes. This reflects our strengths in complex scenarios over single-target cases dominated by strong category cues.

Mixed-dataset training (S+R). Joint training yields further gains on Overall (62.0, best) and Multiple (56.4, best),

improving over the single-dataset setting by +1.0 and +1.1 points, respectively.

4.2.3. Qualitative Results

Fig. 4 shows qualitative grounding results on ScanRefer [9]. **PanoGrounder** accurately localizes the referred objects and produces spatially consistent 3D boxes across diverse scenes and query types. In Fig. 4(a), PanoGrounder correctly distinguishes the target table from distractors by leveraging the phrase “an object with red and black color is placed above it.” Similarly, in Fig. 4(b–d), PanoGrounder resolves challenging references in cluttered scenes by combining attribute cues (e.g., “black”, “white”, “small circular”) with relational/layout cues such as “under the tv”, “under the counter”, and “surrounded by four chairs”. These examples demonstrate that PanoGrounder effectively exploits appearance, geometry, and 3D context from panoramic inputs to handle diverse referring expressions. Additional qualitative examples in Fig. 11 and Fig. 12 further illustrate the robustness of our model.

4.3. Generalization Analysis

Scene Generalization. We evaluate scene-level generalization by testing on two unseen 3D datasets: ARKitScenes [5] paired with human-written expressions from SceneVerse [24], and 3RScan [43] paired with RIORefer [35]. As shown in Table 2, PanoGrounder shows notably smaller performance degradation than existing baselines when transferred to unseen scenes. This indicates

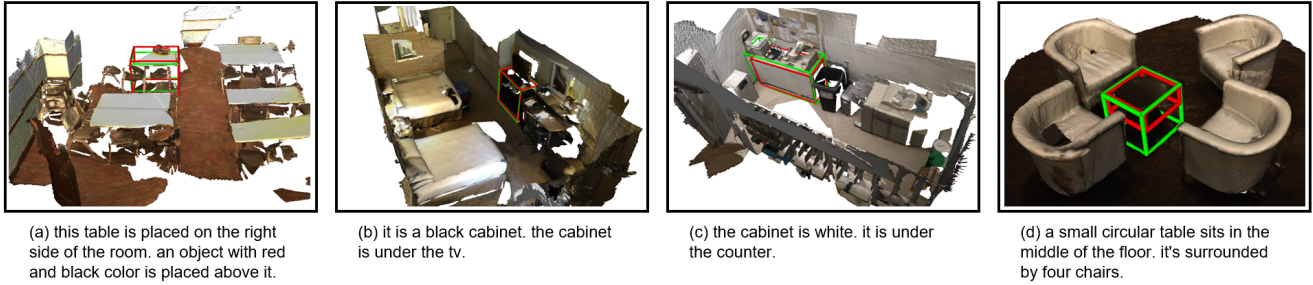


Figure 4. **Qualitative results on ScanRefer [9].** Green boxes denote ground-truth objects, and red boxes denote predictions from PanoGrounder. Across diverse scenes and query types, PanoGrounder produces accurate and spatially consistent grounding results.

Table 2. **Cross-dataset evaluation on ScanNetV2 [11], ARKitScenes [5], and 3RScan [43].** All models are trained on ScanRefer [9] and directly evaluated on unseen 3D scenes from ARKitScenes and 3RScan with corresponding text annotations. To ensure fair comparison focused on 3D scene generalization, we use GT object segmentation for all methods; * additionally leverages ground-truth semantic labels. All baseline results are re-run by us.

Method	ScanRefer			ARKitScenes			3RScan		
	unique	multiple	overall	unique	multiple	overall	unique	multiple	overall
ViL3DRel [10]	92.0	51.8	59.6	57.2	21.1	28.3	71.8	31.3	36.8
3D-VisTA [62]	89.5	49.9	57.2	59.7	26.6	32.9	74.1	32.0	37.7
BUTD-DETR* [22]	92.5	52.6	58.5	66.3	30.6	36.1	—	—	—
MCLN* [39]	93.4	54.9	60.6	61.2	30.0	35.3	—	—	—
Ours	91.7	58.5	64.9	74.2	48.0	53.5	80.4	37.7	43.8

Table 3. **Robustness to ScanRefer [9] text variants.** Acc@0.25 on the original queries and four text modifications (see text for definitions). All models use GT object segmentation; * additionally uses GT semantic labels.

Method	Org.	Rep.	Aff.	Aff. [†]	Mask.
ViL3DRel [10]	59.6	41.5	9.7	6.5	22.9
3D-VisTA [62]	57.2	52.9	50.4	28.3	28.5
BUTD-DETR* [22]	58.5	53.4	55.1	35.5	27.3
MCLN* [39]	60.6	54.6	55.7	35.7	31.5
PQ3D [63]	66.0	63.3	58.6	35.8	33.3
Ours	<u>64.9</u>	<u>61.5</u>	61.3	51.7	41.8
Δ (Ours – PQ3D)	-1.1	-1.8	+2.7	+15.9	+8.5

that our approach generalizes effectively to novel environments and diverse 3D layouts beyond the training distribution. BUTD-DETR [22] and MCLN [39] could not be evaluated on 3RScan+RIORefer because their public implementations are restricted to the ScanNetV2 object set.

Text Generalization. We assess the linguistic robustness of 3D visual grounding models on ScanRefer [9] by generating four variants of each query with LLaMA 3.3 [13]: **Rep.** (rephrase), **Aff.** (affordance/functional description added), **Aff.[†]** (**Aff.** without target nouns), and **Mask.** (tar-

get noun replaced with “object”). To fairly evaluate language understanding independently of proposal quality, we fix proposals to ground-truth object segmentations and re-run all baselines under the same setting.

As shown in Table 3, PanoGrounder performs on par with PQ3D on **Org.** and **Rep.**, and surpasses it on **Aff.** (+2.7). The gains become particularly pronounced once explicit class cues are removed, with improvements of +15.9 on **Aff.[†]** and +8.5 on **Mask..** In these two variants, where the target object name is absent, the model must reason over spatial and contextual cues rather than simple lexical matching. PanoGrounder remains accurate under such implicit or underspecified language, demonstrating strong reasoning and robust performance across diverse textual perturbations.

4.4. Panorama vs. Pinhole Cameras

Panoramic views offer two primary advantages over pinhole cameras: (i) they eliminate the need for viewing direction prediction, thereby simplifying the pipeline; and (ii) they capture the maximum number of text-referenced objects within a single view, strengthening context and relation modeling.

We compare our panoramic representation against several pinhole-based view selection strategies, all using a 120° horizontal FoV and a fixed camera center as in Sec. 3.1. (1) **Fixed rotation (4 / 16 views):** cameras are rotated at

Table 4. **Comparison of panoramic and pinhole view settings.** We report accuracy by view configuration (rows) and by the number of objects referenced in the text (columns). Our panoramic representation substantially outperforms all pinhole baselines without oracle knowledge, and the performance gap widens as the query mentions more surrounding objects. The oracle GT target setting provides an upper bound for pinhole-based approaches.

View setting	Overall	# of objects mentioned in the text				
		0 (0.6%)	1 (23.7%)	2 (46.6%)	3 (21.9%)	4+ (7.2%)
pinhole @ 4 views	41.3	41.1	38.7	42.1	42.0	42.2
pinhole @ 16 views	51.0	50.0	47.3	52.4	51.0	54.5
pinhole @ Semantic [29]	43.6	37.5	42.3	44.3	43.6	44.0
Ours	61.0	49.9	54.7	61.3	64.3	71.0
pinhole @ GT target	67.5	58.9	65.5	69.3	66.5	66.0

Table 5. **Ablation on input modalities and training objectives.** We evaluate the contribution of each input modality (RGB, semantic, geometric) and auxiliary training signals (EMD loss and geometric QA). The full model achieves the best performance.

	Input			Train		Acc@0.25
	RGB	Sem.	Geo.	EMD	Geo QA	
(A)	✓	✗	✗	✗	✗	57.5
(B)	✓	✗	✗	✓	✗	58.4
(C)	✓	✓	✗	✓	✗	60.4
(D)	✓	✓	✓	✓	✗	60.2
(E)	✓	✓	✗	✓	✓	60.7
Ours	✓	✓	✓	✓	✓	61.0

fixed horizontal angular intervals to uniformly cover 360°. (2) **Semantic-based view selection (4 views):** following SeeGround [29], instance masks and predicted labels of Mask3D [42] are used to find text-mentioned objects, up to four of which are chosen by projected size on the panorama, and the camera is oriented toward each; if fewer than four objects are mentioned, the remaining directions are sampled randomly. (3) **GT target (1 view, oracle):** a pinhole camera that always points directly at the ground-truth target.

As shown in Tab. 4, panoramic views substantially outperform all non-oracle pinhole baselines (41.3–51.0 vs. 61.0 overall), indicating that our panoramic representation captures scene context more effectively. The gap further widens as the number of referenced objects increases: in the “4+ objects” category, our approach (71.0) even surpasses the pinhole oracle (66.0). This suggests that pinhole views are fundamentally limited by their narrow field of view, which observes only a subset of objects at once, whereas panoramic views preserve the global spatial relations of the scene.

4.5. Ablation Study

Tab. 5 analyzes how input modalities and auxiliary objectives contribute to performance. Comparing (A) and (B),

adding the EMD loss yields a clear gain (57.5 → 58.4), showing that it provides a useful distance-aware regularization signal. Incorporating semantic features in (C) further boosts accuracy to 60.4, indicating that multi-view fused semantic context is highly beneficial even without geometric input; this trend is also consistent with the qualitative analysis in Fig. 13. The last three rows compare the effect of geometric input and geometric QA: using geometric features without QA (row (D), 60.2) and using geometric QA without geometric input (row (E), 60.7) both fall short of the full model. Our final configuration (**Ours**), which combines RGB, semantic, and geometric features with both EMD and geometric QA, achieves the best accuracy (61.0), suggesting that geometric input and geometric QA act synergistically rather than as interchangeable components.

5. Conclusion

PanoGrounder demonstrates that panoramic (equirectangular) renderings are an effective intermediate representation for 3D visual grounding. They preserve long-range spatial relations within a single view while enabling direct use of powerful 2D VLMs. Extensive experiments show state-of-the-art results on ScanRefer and Nr3D, and strong robustness to unseen scenes and text rephrasings, indicating that panorama-driven VLM grounding is a practical path toward generalizable, open-vocabulary 3D visual grounding tasks.

Limitations and Future Work Two promising directions appear feasible: (i) the framework could be extended to robustly handle queries with *no target object* and *multiple targets* by leveraging the reasoning capabilities of modern VLMs, and (ii) the panorama-driven interface may naturally generalize beyond grounding to *multi-task* settings, such as 3D captioning and 3D VQA, enabling a single model to support broader scene-level understanding and interaction.

Acknowledgments

We thank Chunghyun Park for his helpful comments and technical advice during the development of the model.

References

[1] Eslam Abdelrahman, Mohamed Ayman, Mahmoud Ahmed, Habib Slim, and Mohamed Elhoseiny. Cot3dref: Chain-of-thoughts data-efficient 3d visual grounding. *arXiv preprint arXiv:2310.06214*, 2023. 2

[2] Panos Achlioptas, Ahmed Abdelreheem, Fei Xia, Mohamed Elhoseiny, and Leonidas Guibas. Referit3d: Neural listeners for fine-grained 3d object identification in real-world scenes. In *European conference on computer vision*, pages 422–440, 2020. 1, 2, 5, 6, 3

[3] Peter Anderson, Qi Wu, Damien Teney, Jake Bruce, Mark Johnson, Niko Sünderhauf, Ian Reid, Stephen Gould, and Anton Van Den Hengel. Vision-and-language navigation: Interpreting visually-grounded navigation instructions in real environments. In *Proceedings of the IEEE conference on computer vision and pattern recognition*, pages 3674–3683, 2018. 1

[4] Eslam Bakr, Yasmeen Alsaedy, and Mohamed Elhoseiny. Look around and refer: 2d synthetic semantics knowledge distillation for 3d visual grounding. *Advances in neural information processing systems*, 35:37146–37158, 2022. 2

[5] Gilad Baruch, Zhuoyuan Chen, Afshin Dehghan, Tal Dimry, Yuri Feigin, Peter Fu, Thomas Gebauer, Brandon Joffe, Daniel Kurz, Arik Schwartz, and Elad Shulman. ARKitscenes - a diverse real-world dataset for 3d indoor scene understanding using mobile RGB-d data. In *Thirty-fifth Conference on Neural Information Processing Systems Datasets and Benchmarks Track (Round 1)*, 2021. 2, 5, 6, 7

[6] Ang Cao, Sergio Arnaud, Oleksandr Maksymets, Jianing Yang, Ayush Jain, Ada Martin, Vincent-Pierre Berges, Paul McVay, Ruslan Partsey, Aravind Rajeswaran, Franziska Meier, Justin Johnson, Jeong Joon Park, and Alexander Sax. From thousands to billions: 3d visual language grounding via render-supervised distillation from 2d vlms. In *Proceedings of the 42nd International Conference on Machine Learning*, pages 6505–6521, 2025. 5

[7] Nicolas Carion, Francisco Massa, Gabriel Synnaeve, Nicolas Usunier, Alexander Kirillov, and Sergey Zagoruyko. End-to-end object detection with transformers. In *European conference on computer vision*, pages 213–229. Springer, 2020. 2

[8] Chun-Peng Chang, Shaoxiang Wang, Alain Pagan, and Dider Stricker. Mikasa: Multi-key-anchor & scene-aware transformer for 3d visual grounding. In *Proceedings of the IEEE/CVF Conference on Computer Vision and Pattern Recognition*, pages 14131–14140, 2024. 2, 6, 3

[9] Dave Zhenyu Chen, Angel X Chang, and Matthias Nießner. Scanrefer: 3d object localization in rgb-d scans using natural language. In *European conference on computer vision*, pages 202–221, 2020. 1, 2, 5, 6, 7, 3, 9

[10] Shizhe Chen, Pierre-Louis Guhur, Makarand Tapaswi, Cordelia Schmid, and Ivan Laptev. Language conditioned spatial relation reasoning for 3d object grounding. *Advances in neural information processing systems*, 35:20522–20535, 2022. 2, 6, 7

[11] Angela Dai, Angel X Chang, Manolis Savva, Maciej Halber, Thomas Funkhouser, and Matthias Nießner. Scannet: Richly-annotated 3d reconstructions of indoor scenes. In *Proceedings of the IEEE conference on computer vision and pattern recognition*, pages 5828–5839, 2017. 5, 7

[12] Jacob Devlin, Ming-Wei Chang, Kenton Lee, and Kristina Toutanova. Bert: Pre-training of deep bidirectional transformers for language understanding. In *Proceedings of the 2019 conference of the North American chapter of the association for computational linguistics: human language technologies, volume 1 (long and short papers)*, pages 4171–4186, 2019. 1

[13] Abhimanyu Dubey, Abhinav Jauhri, Abhinav Pandey, Abhishek Kadian, Ahmad Al-Dahle, Aiesha Letman, Akhil Mathur, Alan Schelten, Amy Yang, Angela Fan, et al. The llama 3 herd of models. *arXiv e-prints*, pages arXiv–2407, 2024. 7, 1

[14] Martin A Fischler and Robert C Bolles. Random sample consensus: a paradigm for model fitting with applications to image analysis and automated cartography. *Communications of the ACM*, 24(6):381–395, 1981. 3, 1

[15] Charlie Frogner, Chiyuan Zhang, Hossein Mobahi, Mauricio Araya-Polo, and Tomaso A. Poggio. Learning with a wasserstein loss. In *Advances in Neural Information Processing Systems 28 (NIPS 2015)*, pages 2053–2061, 2015. 5

[16] Rao Fu, Jingyu Liu, Xilun Chen, Yixin Nie, and Wenhan Xiong. Scene-llm: Extending language model for 3d visual reasoning. In *2025 IEEE/CVF Winter Conference on Applications of Computer Vision (WACV)*, pages 2195–2206. IEEE, 2025. 3

[17] Wenxuan Guo, Xiuwei Xu, Ziwei Wang, Jianjiang Feng, Jie Zhou, and Jiwen Lu. Text-guided sparse voxel pruning for efficient 3d visual grounding. In *Proceedings of the Computer Vision and Pattern Recognition Conference*, pages 3666–3675, 2025. 6

[18] Haifeng Huang, Yilun Chen, Zehan Wang, Rongjie Huang, Runsen Xu, Tai Wang, Luping Liu, Xize Cheng, Yang Zhao, Jiangmiao Pang, et al. Chat-scene: Bridging 3d scene and large language models with object identifiers. *Advances in Neural Information Processing Systems*, 37: 113991–114017, 2024. 3, 6

[19] Ronggang Huang, Haoxin Yang, Yan Cai, Xuemiao Xu, Huaidong Zhang, and Shengfeng He. Viewsrd: 3d visual grounding via structured multi-view decomposition. In *Proceedings of the IEEE/CVF International Conference on Computer Vision*, pages 9726–9736, 2025. 2, 6

[20] Shijia Huang, Yilun Chen, Jiaya Jia, and Liwei Wang. Multi-view transformer for 3d visual grounding. In *Proceedings of the IEEE/CVF Conference on Computer Vision and Pattern Recognition*, pages 15524–15533, 2022. 2

[21] Ting Huang, Zeyu Zhang, and Hao Tang. 3d-r1: Enhancing reasoning in 3d vlms for unified scene understanding. *arXiv preprint arXiv:2507.23478*, 2025. 3

[22] Ayush Jain, Nikolaos Gkanatsios, Ishita Mediratta, and Katherine Fragkiadaki. Bottom up top down detection transformers for language grounding in images and point clouds. In *European Conference on Computer Vision*, pages 417–433. Springer, 2022. 2, 6, 7

[23] Ayush Jain, Alexander Swerdlow, Yuzhou Wang, Sergio Arnaud, Ada Martin, Alexander Sax, Franziska Meier, and Ka-

terina Fragkiadaki. Unifying 2d and 3d vision-language understanding. In *Proceedings of the 42nd International Conference on Machine Learning*, pages 26717–26739, 2025. 2, 6

[24] Baoxiong Jia, Yixin Chen, Huangyue Yu, Yan Wang, Xuesong Niu, Tengyu Liu, Qing Li, and Siyuan Huang. Sceneverse: Scaling 3d vision-language learning for grounded scene understanding. In *European Conference on Computer Vision*, pages 289–310, 2024. 2, 5, 6

[25] Bernhard Kerbl, Georgios Kopanas, Thomas Leimkühler, and George Drettakis. 3d gaussian splatting for real-time radiance field rendering. *ACM Trans. Graph.*, 42(4):139–1, 2023. 3, 5

[26] Alexander Kirillov, Eric Mintun, Nikhila Ravi, Hanzi Mao, Chloe Rolland, Laura Gustafson, Tete Xiao, Spencer Whitehead, Alexander C Berg, Wan-Yen Lo, et al. Segment anything. In *Proceedings of the IEEE/CVF international conference on computer vision*, pages 4015–4026, 2023. 4

[27] Suyoung Lee, Jaeyoung Chung, Jaeyoo Huh, and Kyoungh Mu Lee. Odgs: 3d scene reconstruction from omnidirectional images with 3d gaussian splattings. *Advances in Neural Information Processing Systems*, 37:57050–57075, 2024. 1

[28] Martha Lewis, Nihal Nayak, Peilin Yu, Jack Merullo, Qinan Yu, Stephen Bach, and Ellie Pavlick. Does clip bind concepts? probing compositionality in large image models. In *Findings of the Association for Computational Linguistics: EACL 2024*, pages 1487–1500, 2024. 1

[29] Rong Li, Shijie Li, Lingdong Kong, Xulei Yang, and Junwei Liang. Seeground: See and ground for zero-shot open-vocabulary 3d visual grounding. In *Proceedings of the IEEE/CVF Conference on Computer Vision and Pattern Recognition (CVPR)*, 2025. 2, 8

[30] Xiang Li, Jian Ding, Zhaoyang Chen, and Mohamed Elhoseiny. Uni3dl: Unified model for 3d and language understanding. *arXiv preprint arXiv:2312.03026*, 2023. 2

[31] Daizong Liu, Yang Liu, Wencan Huang, and Wei Hu. A survey on text-guided 3-d visual grounding: Elements, recent advances, and future directions. *IEEE Transactions on Neural Networks and Learning Systems*, 2025. 1

[32] Haolin Liu, Anran Lin, Xiaoguang Han, Lei Yang, Yizhou Yu, and Shuguang Cui. Refer-it-in-rgbd: A bottom-up approach for 3d visual grounding in rgbd images. In *Proceedings of the IEEE/CVF Conference on Computer Vision and Pattern Recognition*, pages 6032–6041, 2021. 2

[33] Haotian Liu, Chunyuan Li, Qingyang Wu, and Yong Jae Lee. Visual instruction tuning. *Advances in neural information processing systems*, 36:34892–34916, 2023. 1, 3

[34] Junyu Luo, Jiahui Fu, Xianghao Kong, Chen Gao, Haibing Ren, Hao Shen, Huaxia Xia, and Si Liu. 3d-sps: Single-stage 3d visual grounding via referred point progressive selection. In *Proceedings of the IEEE/CVF Conference on Computer Vision and Pattern Recognition*, pages 16454–16463, 2022. 2

[35] Taiki Miyanishi, Daichi Azuma, Shuhei Kurita, and Motoaki Kawanabe. Cross3dvg: Cross-dataset 3d visual grounding on different rgb-d scans. In *2024 International Conference on 3D Vision (3DV)*, pages 717–727. IEEE, 2024. 2, 5, 6

[36] Timothy Niven and Hung-Yu Kao. Probing neural network comprehension of natural language arguments. In *Proceedings of the 57th Annual Meeting of the Association for Computational Linguistics*, pages 4658–4664, Florence, Italy, 2019. Association for Computational Linguistics. 1

[37] Maxime Oquab, Timothée Darcet, Theo Moutakanni, Huy V. Vo, Marc Szafraniec, Vasil Khalidov, Pierre Fernandez, Daniel Haziza, Francisco Massa, Alaeldin El-Nouby, Russell Howes, Po-Yao Huang, Hu Xu, Vasu Sharma, Shang-Wen Li, Wojciech Galuba, Mike Rabbat, Mido Assran, Nicolas Ballas, Gabriel Synnaeve, Ishan Misra, Herve Jegou, Julien Mairal, Patrick Labatut, Armand Joulin, and Piotr Bojanowski. Dinov2: Learning robust visual features without supervision, 2023. 2, 4, 1

[38] Charles R Qi, Or Litany, Kaiming He, and Leonidas J Guibas. Deep hough voting for 3d object detection in point clouds. In *proceedings of the IEEE/CVF International Conference on Computer Vision*, pages 9277–9286, 2019. 2

[39] Zhipeng Qian, Yiwei Ma, Zhekai Lin, Jiayi Ji, Xiawu Zheng, Xiaoshuai Sun, and Rongrong Ji. Multi-branch collaborative learning network for 3d visual grounding. In *European Conference on Computer Vision*, pages 381–398. Springer, 2024. 2, 6, 7

[40] Alec Radford, Jong Wook Kim, Chris Hallacy, Aditya Ramesh, Gabriel Goh, Sandhini Agarwal, Girish Sastry, Amanda Askell, Pamela Mishkin, Jack Clark, et al. Learning transferable visual models from natural language supervision. In *International conference on machine learning*, pages 8748–8763. PMLR, 2021. 1, 3

[41] Siyu Ren, Zhiyong Wu, and Kenny Q Zhu. Emo: Earth mover distance optimization for auto-regressive language modeling. In *ICLR*. ICLR, 2024. 5

[42] Jonas Schult, Francis Engelmann, Alexander Hermans, Or Litany, Siyu Tang, and Bastian Leibe. Mask3D: Mask Transformer for 3D Semantic Instance Segmentation. 2023. 8

[43] Johanna Wald, Armen Avetisyan, Nassir Navab, Federico Tombari, and Matthias Nießner. Rio: 3d object instance re-localization in changing indoor environments. In *Proceedings of the IEEE/CVF International Conference on Computer Vision*, pages 7658–7667, 2019. 2, 5, 6, 7

[44] Weihan Wang, Qingsong Lv, Wenmeng Yu, Wenyi Hong, Ji Qi, Yan Wang, Junhui Ji, Zhuoyi Yang, Lei Zhao, Song XiXuan, et al. Cogvilm: Visual expert for pretrained language models. *Advances in Neural Information Processing Systems*, 37:121475–121499, 2024. 1, 5

[45] Xuezhi Wang, Jason Wei, Dale Schuurmans, Quoc Le, Ed Chi, Sharan Narang, Aakanksha Chowdhery, and Denny Zhou. Self-consistency improves chain of thought reasoning in language models. In *Proceedings of the 11th International Conference on Learning Representations (ICLR 2023)*, 2023. 5

[46] Yuan Wang, Yali Li, and Shengjin Wang. G[^] 3-lq: Marrying hyperbolic alignment with explicit semantic-geometric modeling for 3d visual grounding. In *Proceedings of the IEEE/CVF Conference on Computer Vision and Pattern Recognition*, pages 13917–13926, 2024. 2

[47] Yuan Wang, Ya-Li Li, WU Eastman ZY, and Shengjin Wang. Liba: Language instructed multi-granularity bridge assistant

for 3d visual grounding. In *Proceedings of the AAAI Conference on Artificial Intelligence*, pages 8114–8122, 2025. 2, 6

[48] Yanmin Wu, Xinhua Cheng, Renrui Zhang, Zesen Cheng, and Jian Zhang. Eda: Explicit text-decoupling and dense alignment for 3d visual grounding. In *Proceedings of the IEEE/CVF conference on computer vision and pattern recognition*, pages 19231–19242, 2023. 2

[49] Runsen Xu, Zhiwei Huang, Tai Wang, Yilun Chen, Jiangmiao Pang, and Dahua Lin. Vlm-grounder: A vlm agent for zero-shot 3d visual grounding. In *CoRL*, 2024. 2

[50] Jianing Yang, Xuweiyi Chen, Shengyi Qian, Nikhil Madaan, Madhavan Iyengar, David F Fouhey, and Joyce Chai. Llm-grounder: Open-vocabulary 3d visual grounding with large language model as an agent. In *2024 IEEE International Conference on Robotics and Automation (ICRA)*, pages 7694–7701. IEEE, 2024. 2

[51] Zhengyuan Yang, Songyang Zhang, Liwei Wang, and Jiebo Luo. Sat: 2d semantics assisted training for 3d visual grounding. In *Proceedings of the IEEE/CVF International Conference on Computer Vision*, pages 1856–1866, 2021. 2

[52] Zhihao Yuan, Xu Yan, Yinghong Liao, Ruimao Zhang, Sheng Wang, Zhen Li, and Shuguang Cui. Instancerefer: Cooperative holistic understanding for visual grounding on point clouds through instance multi-level contextual referring. In *Proceedings of the IEEE/CVF International Conference on Computer Vision*, pages 1791–1800, 2021. 2

[53] Zhihao Yuan, Jinke Ren, Chun-Mei Feng, Hengshuang Zhao, Shuguang Cui, and Zhen Li. Visual programming for zero-shot open-vocabulary 3d visual grounding. In *Proceedings of the IEEE/CVF Conference on Computer Vision and Pattern Recognition*, pages 20623–20633, 2024. 2

[54] Yuanwen Yue, Anurag Das, Francis Engelmann, Siyu Tang, and Jan Eric Lenssen. Improving 2d feature representations by 3d-aware fine-tuning. In *European Conference on Computer Vision*, pages 57–74. Springer, 2024. 1

[55] Mert Yuksekgonul, Federico Bianchi, Pratyusha Kalluri, Dan Jurafsky, and James Zou. When and why vision-language models behave like bags-of-words, and what to do about it? In *International Conference on Learning Representations*, 2023. 1

[56] Yang Zhan, Yuan Yuan, and Zhitong Xiong. Mono3dvg: 3d visual grounding in monocular images. In *Proceedings of the AAAI Conference on Artificial Intelligence*, pages 6988–6996, 2024. 2

[57] Honghua Zhang, Liunian Harold Li, Tao Meng, Kai-Wei Chang, and Guy Van den Broeck. On the paradox of learning to reason from data. In *Proceedings of the 32nd International Joint Conference on Artificial Intelligence (IJCAI)*, pages 3365–3373, 2023. 1

[58] Lvmin Zhang, Anyi Rao, and Maneesh Agrawala. Adding conditional control to text-to-image diffusion models. In *Proceedings of the IEEE/CVF international conference on computer vision*, pages 3836–3847, 2023. 2, 4

[59] Chenming Zhu, Tai Wang, Wenwei Zhang, Kai Chen, and Xihui Liu. Scanreason: Empowering 3d visual grounding with reasoning capabilities. In *European Conference on Computer Vision*, pages 151–168. Springer, 2024. 2

[60] Chenming Zhu, Tai Wang, Wenwei Zhang, Jiangmiao Pang, and Xihui Liu. Llava-3d: A simple yet effective pathway to empowering lmms with 3d capabilities. In *Proceedings of the IEEE/CVF International Conference on Computer Vision*, pages 4295–4305, 2025. 3, 6

[61] Yihang Zhu, Jinhao Zhang, Yuxuan Wang, Aming Wu, and Cheng Deng. Vgmamba: Attribute-to-location clue reasoning for quantity-agnostic 3d visual grounding. In *Proceedings of the IEEE/CVF International Conference on Computer Vision*, pages 5295–5304, 2025. 6

[62] Ziyu Zhu, Xiaojian Ma, Yixin Chen, Zhidong Deng, Siyuan Huang, and Qing Li. 3d-vista: Pre-trained transformer for 3d vision and text alignment. In *Proceedings of the IEEE/CVF International Conference on Computer Vision*, pages 2911–2921, 2023. 2, 5, 6, 7, 3

[63] Ziyu Zhu, Zhuofan Zhang, Xiaojian Ma, Xuesong Niu, Yixin Chen, Baoxiong Jia, Zhidong Deng, Siyuan Huang, and Qing Li. Unifying 3d vision-language understanding via promptable queries. In *European Conference on Computer Vision*, pages 188–206, 2024. 2, 5, 6, 7, 3

PanoGrounder: Bridging 2D and 3D with Panoramic Scene Representations for VLM-based 3D Visual Grounding

Supplementary Material

A. Implementation Details

A.1. Camera Placement and Rendering Stage

In this section, we further elaborate on how we select panoramic viewpoints across scenes and render color, range, and feature maps from each viewpoint.

Floor estimation and candidate grid. We estimate the floor plane using RANSAC [14]. Specifically, we downsample the point cloud (mesh vertices or 3DGS centers) to a 5 cm resolution, retain the bottom 50% of points based on height as floor candidates, and run 10,000 RANSAC iterations. At each iteration, we sample three points to fit a plane, enforce a nearly vertical normal ($|n_z| > 0.9$), and count inliers within a threshold of 10^{-3} m, ultimately selecting the plane with the highest inlier count.

Subsequently, we compute a 2D convex hull over all scene points to obtain a tight floor footprint and create a 2D grid over this hull with a spacing of $h=0.1$ m. The z -coordinates of the grid centers are set to the average height of the raw camera poses.

A.2. Multi-Modal Panorama

We provide specific implementation details for constructing the multi-modal panoramic representations described in Sec. 3.2.

Rendering Configuration and Dimensions. All panoramic inputs are generated using Equirectangular Projection (ERP) with a 360° horizontal and 180° vertical field of view. We differentiate the rendering resolution based on the modality:

- **RGB and Depth:** Rendered at $(H, W) = (490, 490)$. These are subsequently processed with a patch size of 14×14 , resulting in a flattened token sequence of length $N_f = 1225$ (corresponding to a 35×35 grid).
- **Semantic Features:** Rendered directly at the target resolution of 35×35 to align with the token grid without further patching.

Regarding the underlying 3D representations, we utilize PyTorch3D for mesh-based scenes and ODGS [27] for 3D Gaussian Splatting (3DGS) scenes.

Feature Extraction Details. The geometric and semantic feature maps are constructed as follows:

- **Geometric Features (\mathbf{f}_{geo}):** The rendered depth map $D_s \in \mathbb{R}^{490 \times 490}$ is first clipped and min-max normalized to $[0, 1]$. This normalized map is fed into a lightweight

ViT encoder (trainable DINOv2 [37]) with a patch size of 14, outputting $\mathbf{f}_{\text{geo}} \in \mathbb{R}^{N_f \times d_{\text{geo}}}$ ($d_{\text{geo}} = 384$).

- **Semantic Features (\mathbf{f}_{sem}):** We first extract raw feature maps from a frozen ViT encoder applied to the original RGB views. These raw features are bilinearly interpolated to the resolution of the original RGB images. The upsampled features are then lifted to 3D: for mesh scenes, we project per-pixel features onto vertices using camera parameters; for 3DGS scenes, we adopt [54] to lift features onto Gaussians. Finally, the aggregated 3D semantic field is rendered directly at the 35×35 resolution, yielding $\mathbf{f}_{\text{sem}} \in \mathbb{R}^{N_f \times d_{\text{sem}}}$ ($d_{\text{sem}} = 384$).

A.3. Prompt Design

To clearly define the role of the VLM and enforce a consistent output format, we encapsulate the original referring expressions from the dataset within a concise instruction-style prompt. Fig. 5(a) illustrates the specific prompt template employed in the ScanRefer experiments. Furthermore, to evaluate text generalization (Sec. 4.3), we leverage LLaMA 3.3 [13] to generate linguistic variants of the original queries, specifically focusing on rephrasing and affordance-based descriptions. We designed three distinct instruction prompts for these text modifications, as depicted in Fig. 5(b)–(d).

- **Masking.** We substitute instances of the ground-truth class label in the text with a generic placeholder “object”, while preserving the remainder of the sentence structure.
- **Rephrasing.** Utilizing the instruction prompt in Fig. 5(b), LLaMA 3.3 paraphrases the sentence to alter its syntax and vocabulary, ensuring that the semantic context and constraints associated with the target object remain intact.
- **Affordance.** Guided by the prompt in Fig. 5(c), LLaMA 3.3 generates a first-person description emphasizing the intended interaction with the target object (i.e., affordance), while maintaining all original constraints.
- **Affordance (no name).** Using the prompt in Fig. 5(d), the model follows a similar affordance-focused instruction but is explicitly restricted from naming the target object’s class label or its near-synonyms. Consequently, the query relies exclusively on functional descriptions and contextual cues.

A.4. VLM Hyperparameters

In this section, we detail the hyperparameters used for training and inference of the VLM. We fine-tune the backbone

(a) Prompt used for querying PanoGrounder

Please locate the object described as: <description>. If there are multiple, pick the most prominent. Provide the bounding box coordinates as [x1,y1,x2,y2]. Output only the coordinates.

(b) Prompt for generating rephrased queries

You are a precise paraphraser. Rewrite the given sentence so that the meaning is exactly the same, but the wording and phrasing are different. Do NOT add or remove any information. Keep entities, counts, colors, and spatial relations unchanged.

<description>.

(c) Prompt for generating affordance-based queries

You are an affordance-based rewriter. Goal: Describe what the speaker wants to DO with the implied target object. Use first-person language ("I want to ...", "I need to ...", "I'd like to ..."). Keep ALL constraints (attributes like color/size, counts, spatial relations such as left/right/behind/between/next to/in front of/inside, and references to nearby items) EXACTLY the same; you may reorder or use synonyms. Do NOT add or remove information. IMPORTANT: Pick an action that is TYPICAL for the correct answer word (object affordance). AVOID generic verbs unless they are the prototypical affordance for that object type.

<description>.

(d) Prompt for generating affordance-based queries (no name)

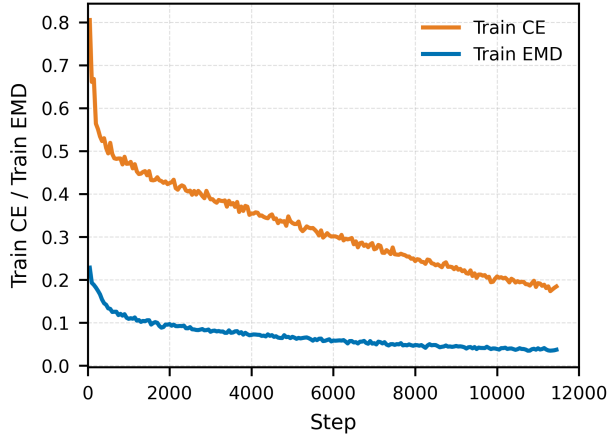
You are an affordance-based rewriter. Goal: Describe what the speaker wants to DO with the implied target object, WITHOUT ever naming that object or any of its synonyms. Use first-person language ("I want to ...", "I need to ...", "I'd like to ..."). Keep ALL constraints (attributes like color/size, counts, spatial relations such as left/right/behind/between/next to/in front of/inside, and references to nearby items) EXACTLY the same; you may reorder or use synonyms. Do NOT add or remove information. IMPORTANT: Pick an action that is TYPICAL for the correct answer word (object affordance). AVOID generic verbs unless they are the prototypical affordance for that object type. NEVER name the target object or any near-synonyms.

<description>.

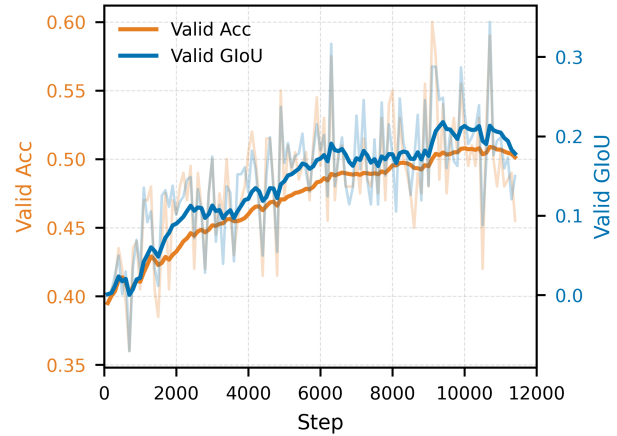
Figure 5. **Prompt templates for VLM inference and text augmentation.** (a) Instruction-style prompt for querying PanoGrounder with a panoramic image and a referring expression <description>. (b) LLaMA 3.3 prompt for rephrasing queries while preserving the original semantic meaning. (c) LLaMA 3.3 prompt for generating affordance-focused descriptions that explicitly include the object class name. (d) LLaMA 3.3 prompt for generating affordance-focused descriptions that exclude the object class name, so that target is specified only through its affordances and context.

using Low-Rank Adaptation (LoRA) with a rank of $r = 64$ and $\alpha = 64$. The model is trained for 5 epochs on the ScanRefer dataset with a batch size of 64, utilizing the Adam optimizer with a learning rate of 1×10^{-4} . Given that multiple cameras are deployed in a single scene, the training set size for each query text expands according to

the number of camera viewpoints. Consequently, a single epoch entails approximately $2.4 \times$ more iterations compared to the standard ScanRefer or ReferIt3D benchmarks. During training, if the ground-truth object is not visible in a specific panoramic image, that sample is excluded from the batch. For the supervision signal, the Earth Mover's Dis-



(a) Training CE and EMD loss curves.



(b) Validation accuracy and GIoU during training.

Figure 6. **Training dynamics of our model.** (a) Training losses (CE and EMD) consistently decrease and stabilize, showing smooth optimization behavior. (b) Validation Acc and GIoU are optimized during training and eventually converge as the number of steps increases.

tance (EMD) loss is calculated based on coordinates normalized by the maximum output image coordinate (999), and its weight is set to $\lambda = 10.0$.

Furthermore, we incorporate auxiliary Geometric QA samples into the training pipeline, which constitute 1/3 of the total data. While the main text describes range-based comparisons, we essentially augment these tasks to include spatial ranking queries along the x , y , and z axes. Crucially, these auxiliary samples require no human annotation and are generated on-the-fly during the data loading process.

B. Two-Stage Variant

Two-stage methods follow a proposal-and-selection strategy. In the ReferIt3D [2] benchmark, the task inherently provides candidate ground-truth (GT) point cloud segments. Similarly, for the modified ScanRefer evaluation (Sec. 4.3), to ensure a fair comparison against existing baselines [8, 62, 63] that rely on varying segmentors, we utilize GT masks for all methods.

The inference pipeline operates as follows: The 2D VLM first processes the equirectangular panorama to predict a 2D bounding box. We then match this prediction to a specific 3D instance by computing the IoU with the projected GT instance masks, assigning the prediction to the instance with the highest IoU.

Finally, we aggregate these frame-level predictions into a single decision. For ScanRefer, we utilize standard majority voting. For ReferIt3D, leveraging the known candidate geometries, we employ a weighted voting scheme based on the visible proportion of each candidate in the frame, thereby favoring viewpoints where the target is more clearly observable.

Table 6. Ablation on camera placement strategy. The *Random* baseline is constrained to use the same number of cameras as our method for each scene.

	RC	DS	DT	Avg. Cameras / Scene	Acc@0.25
Random	✗	✗	✗	2.4	51.9
(a)	✓	✗	✗	2.5	55.7
(b)	✓	✓	✗	2.4	59.2
Ours	✓	✓	✓	2.4	61.0

C. Training Convergence

Fig. 6(a) illustrates the training Cross-Entropy (CE) loss and Earth Mover’s Distance (EMD) loss. Both losses decrease steadily without noticeable instability or divergence, confirming that the combined objective provides stable gradients and that the optimization process converges reliably. Fig. 6(b) shows the evolution of validation accuracy and validation GIoU over training steps. Both metrics improve at the beginning of training and then gradually saturate, indicating that the model learns effective localization behavior and subsequently converges. In practice, our model converges after roughly 5 epochs (approximately 10,000 optimization steps).

D. Additional Ablation Studies

In this section, we provide additional ablation studies to further evaluate the effectiveness of various components of our method. Unless otherwise noted, all ablation studies are conducted on ScanRefer [9] and report Acc@0.25.

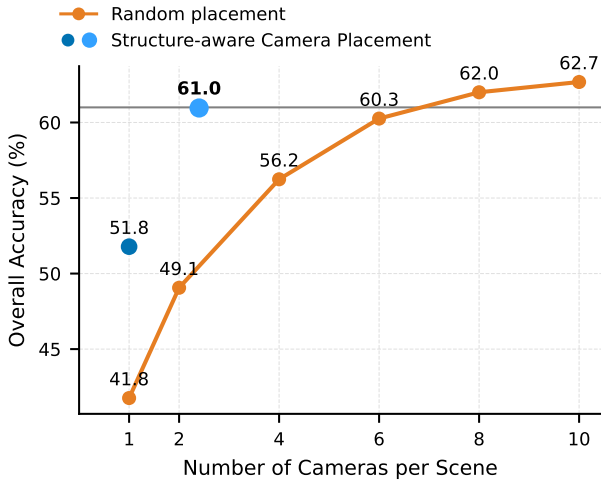


Figure 7. Effect of the number of cameras per scene on overall accuracy. The orange curve shows random placement, whose performance monotonically increases as more cameras are placed in the scene. Blue markers denote our Structure-aware Camera Placement: the left marker corresponds to the best single-camera configuration, and the right marker corresponds to our full model with an average of only 2.4 cameras per scene, which achieves overall accuracy roughly equivalent to using about 7 randomly placed cameras.

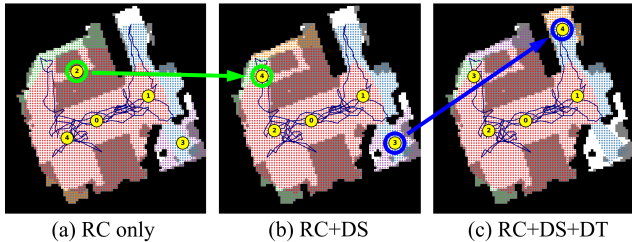


Figure 8. Effect of camera placement factors. Top-down views of a scene where white cells show the floor layout, gray cells denote obstacles, and the blue curve depicts the raw RGB camera trajectory. Yellow numbered markers indicate selected panoramic cameras, and the colored dots around each camera visualize the ray coverage contributed by that camera. Comparing the green circles in (a) and (b), adding distance-to-surface (RC+DS) moves cameras away from obstacles into more open regions. Comparing the blue circles in (b) and (c), further adding distance-to-trajectory (RC+DS+DT) keeps cameras near the original capture path while still achieving good coverage.

D.1. Structure-aware Camera Placement

Tab. 6 and Fig. 8 present an ablation study of the scoring factors employed in our *structure-aware camera placement* module. While using only ray coverage (RC) improves upon random selection, cameras may still be positioned too close to obstacles. In Fig. 8(a), the green circle marks a

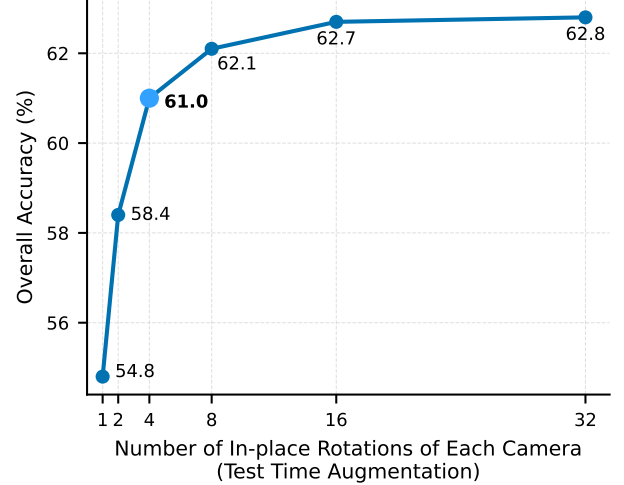


Figure 9. Effect of test-time in-place rotations. We evaluate how many in-place rotations per camera are used for test-time augmentation. Performance increases rapidly from 1 to 4 rotations, and gradually saturates beyond 8, indicating that **four** rotations provide the best balance between performance and computational cost.

viewpoint located directly on top of the sofa in the top-left region. By incorporating the distance-to-surface factor (RC+DS), as shown in (b), the corresponding viewpoint (green circle) is shifted away from the sofa and slightly outward. This adjustment prevents distortion near the bottom of the panorama and yields a significant accuracy gain (55.7 \rightarrow 59.2). However, RC+DS may still place cameras in geometrically incomplete areas; the blue circle in (b) highlights a viewpoint inside the bathroom—a region the ground-truth trajectory never enters—resulting in incomplete reconstruction. Our full strategy (RC+DS+DT) additionally incorporates the distance-to-trajectory factor to discourage placement in such out-of-trajectory regions. Consequently, the blue circle in (c) shows this viewpoint shifted back toward the main path near the kitchen, effectively filling the remaining uncovered space. This configuration achieves optimal scene coverage and rendering quality, reaching the highest grounding accuracy with a comparable number of cameras per scene.

Fig. 7 illustrates the effect of the number of cameras per scene. With random placement, overall accuracy increases monotonically as more cameras are added, though the incremental gain diminishes as the scene becomes saturated with views. Our Structure-aware Camera Placement provides two key reference points (blue markers): (i) the best single-view, which selects the single camera with the highest score and significantly outperforms the random single-view baseline; and (ii) the full-selection, averaging 2.4 cameras per scene, which achieves an overall accuracy comparable to that of approximately seven randomly placed cameras. This

Table 7. **Impact of scene representation: triangle mesh vs 3D Gaussian Splatting (3DGS) [25].** We instantiate our framework with either a mesh-based renderer or a 3DGS representation, and compare performance on Nr3D [2] and ScanRefer [9]. All other components are kept identical. For Nr3D, we report accuracy on the Easy/Hard and View-Dependent/Independent (VD/VID) splits as well as Overall; for ScanRefer, we report Accuracy@0.25 (IoU) on the Unique, Multiple, and Overall splits.

Method	Nr3D					Sr3D					ScanRefer		
	Easy	Hard	VD	VID	Overall	Easy	Hard	VD	VID	Overall	Unique	Multiple	Overall
LIFT-GS [6]	—	—	—	—	—	—	—	—	—	—	—	—	49.7
Ours (3DGS)	81.8	61.0	67.3	72.9	71.2	77.5	68.0	59.3	75.4	74.7	82.5	53.7	59.3
Ours (Mesh)	82.2	67.2	70.5	76.3	74.6	81.3	74.2	60.5	80.0	79.1	84.3	55.3	61.0

demonstrates that our strategy substantially improves both overall accuracy and computational efficiency.

D.2. Adapter Initialization

We investigate the impact of using a zero-initialized convolution layer within the Multi-modal Feature Adapter. This ablation study was conducted using only the multi-view semantic feature encoder, excluding the geometry encoder and Geometric QA. We observe that replacing the zero-initialization of the 1×1 convolution layer with Gaussian initialization degrades performance to 59.5%, falling short of the baseline adapter configuration which achieves 60.4%. The baseline configuration, combining a 2-layer MLP with a zero-initialized 1×1 convolution, highlights the importance of this initialization strategy. Zero initialization helps preserve the pretrained VLM behavior while enabling the adapter to effectively learn task-specific context.

D.3. Test Time Augmentation

As introduced in Sec. 4.1, our inference pipeline employs test-time augmentation by rendering multiple panoramas from each camera location with fixed yaw intervals. In this section, we analyze the efficacy of this strategy and justify our design choice of performing four 90° rotations.

Fig. 9 illustrates the impact of increasing the number of yaw rotations on accuracy. Performance improves significantly with fewer rotations and continues to rise until approximately 4–8 rotations, beyond which the gains saturate. This trend indicates that **four** in-place rotations offer the optimal trade-off between accuracy improvement and computational cost.

This approach can be interpreted through the lens of *self-consistency* [45], where agreement across multiple perturbed inputs serves as a proxy for confidence. By feeding the VLM with multiple panoramas rendered from different yaw angles at the same location, we assess the reliability of the predictions based on the consistency of the model’s outputs.

D.4. Scene representation

For all experiments, we assume that each scene is available as a renderable 3D representation capable of storing and querying per-point or per-surface features. We implement this representation using either a triangle mesh or a 3D Gaussian Splatting (3DGS) model [25], training each variant on panoramas rendered from its respective representation. As shown in Tab. 7, the mesh-based representation outperforms the 3DGS model across all benchmarks. However, our 3DGS-based model still surpasses LIFT-GS [6], the only existing 3D visual grounding model built upon 3DGS.

As shown in Fig. 10, we observe distinct characteristics between the mesh and 3DGS representations within our framework. While the mesh provides more stable rendering, 3DGS excels in visual fidelity, surface completeness (i.e., hole-filling), and reconstruction of distant regions. For instance, in scenes such as `scene0000_00`, 3DGS demonstrates superior surface continuity (e.g., on the floor) and sharper object boundaries (e.g., pictures on the wall). Similarly, in `scene0300_00`, 3DGS successfully reconstructs distant areas that the mesh model fails to capture. Conversely, in scenes with incomplete reconstructions (e.g., `scene0008_00` and `scene0623_00`), 3DGS models are prone to artifacts, which degrades rendering quality.

Although 3DGS enables photorealistic view synthesis, we hypothesize that this advantage is attenuated in our setting. Since the VLM utilizes resized panoramas at a 490×490 resolution, the benefits of high-frequency fidelity are marginalized. In contrast, reconstruction artifacts and blurry regions inherent to 3DGS can corrupt the semantic and geometric feature maps processed by the 2D VLM, thereby impairing 3D reasoning. Nevertheless, supporting 3DGS rendering remains practically significant, as it allows our framework to operate directly on 3DGS reconstructions, obviating the need for mesh conversion or manual cleaning.

E. Qualitative Results

Qualitative comparisons are conducted on the ScanRefer dataset [9]. Fig. 11 shows representative success

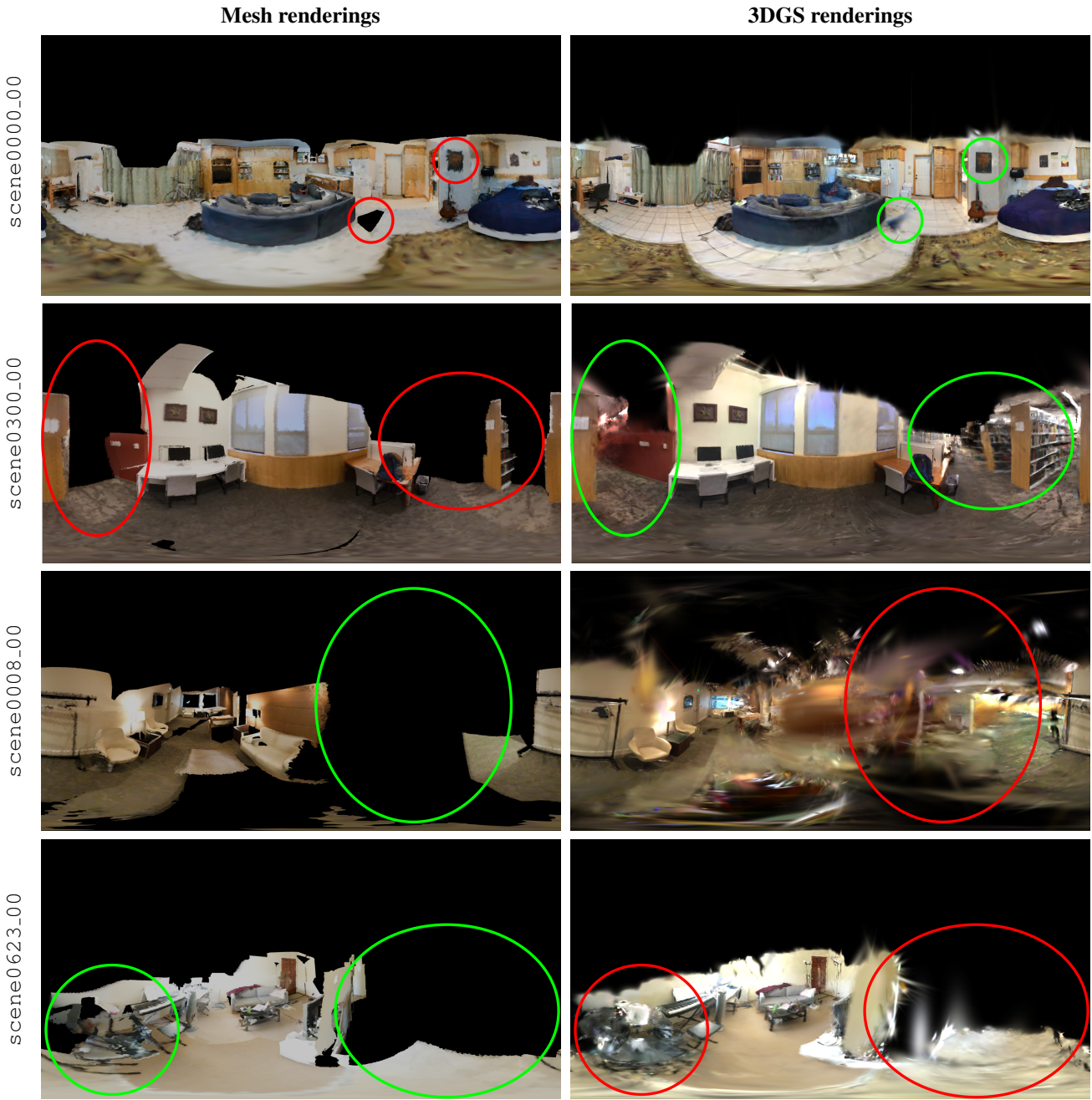


Figure 10. Mesh vs 3DGS panoramic renderings across different scenes.

cases where PanoGrounder closely matches the ground-truth bounding boxes. Across a variety of room types (kitchens, bathrooms, offices, and bedrooms), the predicted boxes (red) align well with the ground-truth boxes (green), even when the target object is small (e.g., Fig. 11(f), (h)). Many of the queries require understanding relational cues such as “A next to B” or “A above B”. These examples illustrate that PanoGrounder can reliably parse such contextual descriptions and ground them to the correct instance in 3D.

Fig. 12 compares PanoGrounder with 3D-VisTA [62] under identical input conditions, where both methods receive the same ground-truth instance masks. 3D-VisTA (red boxes) often locks onto a plausible but incorrect instance or drifts to a nearby distractor. In contrast, thanks to the pre-trained knowledge of the underlying VLM, PanoGrounder is robust on rare objects, such as those in Fig. 12(c), (j). These qualitative results echo our quantitative findings, showing that combining panoramic context with pretrained

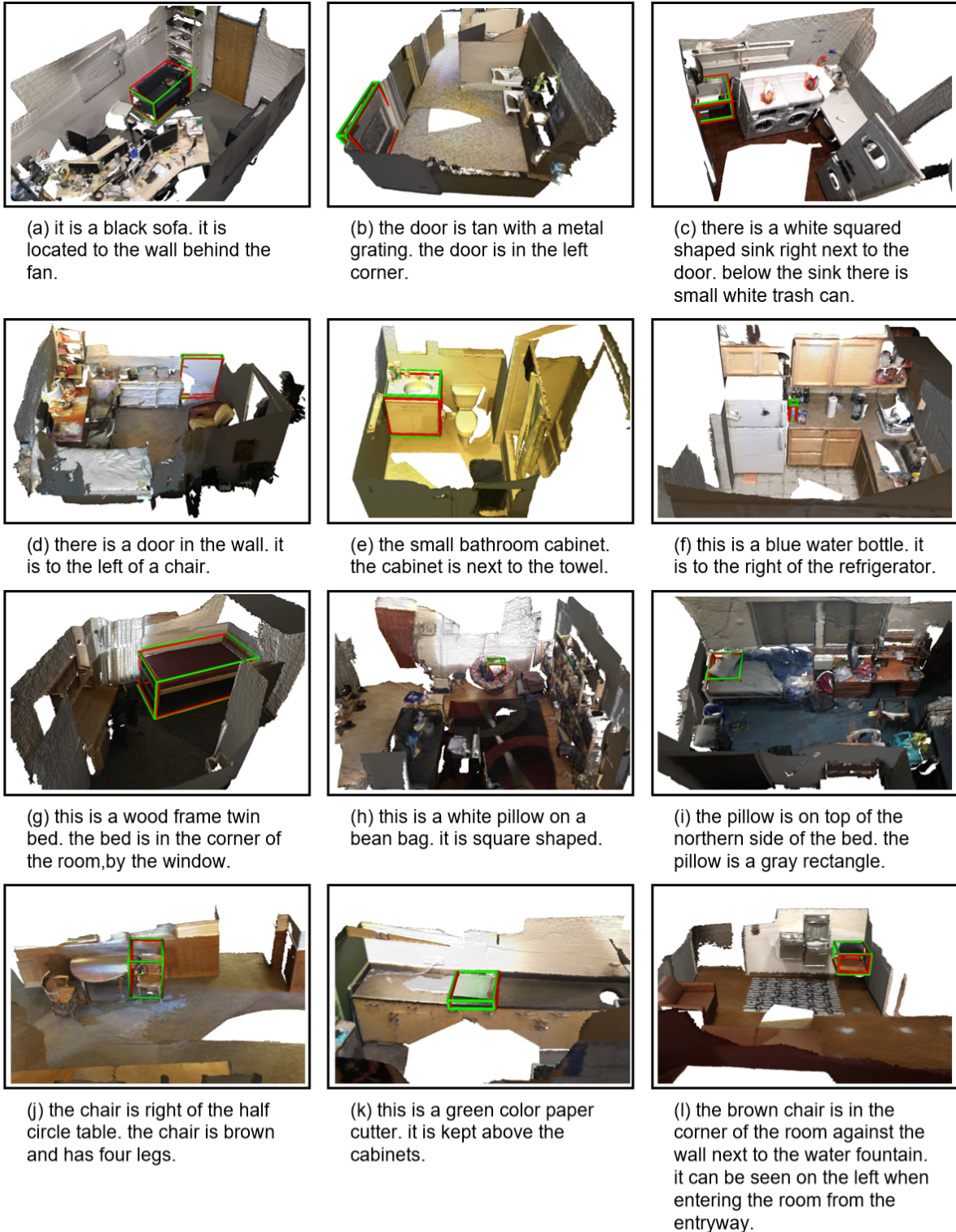


Figure 11. **Qualitative comparison with ground-truth bounding boxes.** In these examples, PanoGrounder (red boxes) produces the correct localization, similar to ground-truth boxes (green boxes).

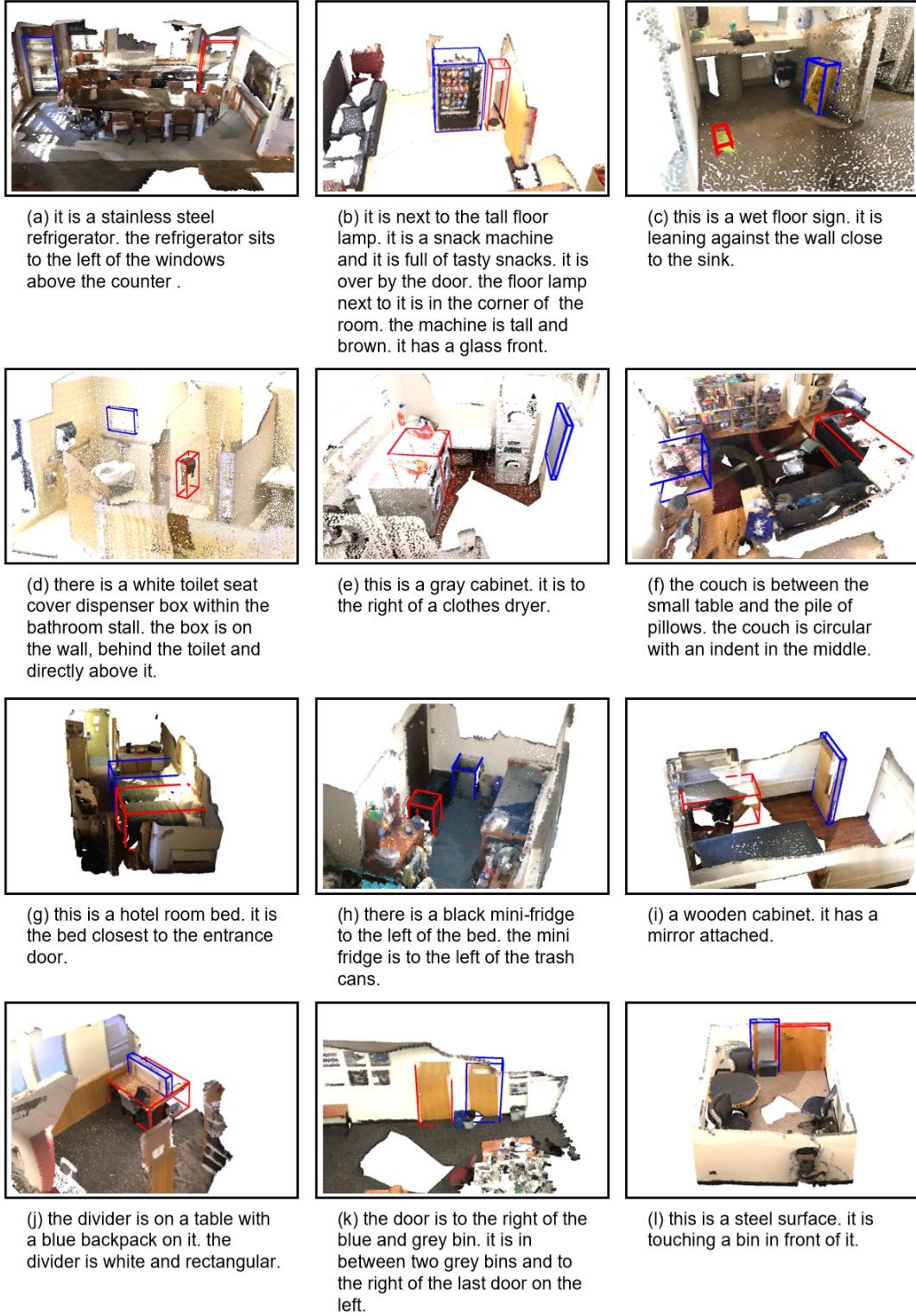


Figure 12. **Qualitative comparison with 3D-VisTA.** Both methods are provided with the same ground-truth instance masks for fair input conditions. In these examples, PanoGrounder (blue boxes) produces the correct localization, while 3D-VisTA (red boxes) yields an incorrect bounding box.



(a) this is a kitchen cabinet. it sets along the wall, waiting to have stuff stored in it.

(b) this is a square printer. it is in front of the window.

(c) this is a black backpack. to the left of it is a recliner chair.

(d) there is a rectangular black trash can. it is next to a door.

Figure 13. **Raw 2D predictions from PanoGrounder with and without semantic features.** Green boxes show ground truth, blue boxes show predictions with semantic features, and red boxes show predictions without features.

VLM leads to more robust and precise 3D visual grounding.

E.1. Effect of Features

In Fig. 13, we compare raw 2D predictions from PanoGrounder when it is run on the RGB alone (red) versus when we augment it with our semantic features (blue). In all four examples, the blue boxes align closely with the ground-truth boxes (green), while the red boxes often drift to a nearby but incorrect region. This shows that the semantic features provide strong additional cues beyond the RGB appearance of the equirectangular image.

In Fig. 13(a), the kitchen cabinet is seen from an oblique angle and is partially occluded, making it difficult to distinguish from nearby structures using appearance alone; with semantic features, PanoGrounder localizes the correct cabinet region. In Fig. 13(b), the scene is extremely dark and the printer is barely visible, so the RGB-only prediction snaps to a nearby larger object that is easier to see, whereas the semantic features guide the model toward the true printer location. Finally, in Fig. 13(d), the referred trash can is small and far from the camera; the baseline is attracted to a nearby large distractor, while the semantic features guide the prediction to the correct instance next to the door. Overall, these cases illustrate that semantic features make PanoGrounder substantially more robust to occlusion, illumination changes, textural clutter, and tiny targets.

F. Runtime Analysis

On the ScanRefer [9] validation split, we measure the wall-clock time required to answer a single text query at inference. For each scene, we select on average 2.4 cameras, and for each camera we render four yaw-rotated panoramas, leading to $2.4 \times 4 = 9.6$ PanoGrounder forward passes per query. In our hardware setup, up to 16 panoramas can be processed in a single batched PanoGrounder inference on a single NVIDIA A100 GPU, which amortizes the per-query computation cost.

Since camera placement and panoramic rendering are performed as an offline preprocessing step, we only time the online components: PanoGrounder inference and visibility-aware 3D aggregation. Averaged over the entire validation

set, PanoGrounder inference takes 3.09s per query and the subsequent 3D aggregation adds 0.21s, resulting in a total online runtime of 3.30s per text query.